



Local oscillator port integrated resonator for Rydberg atom-based electric field measurement enhancement

Bo Wu¹, Dunwei Liao¹, Zhenke Ding¹, Kai Yang¹, Yi Liu¹, Di Sang¹, Qiang An¹ and Yunqi Fu^{1*}

*Correspondence:

yunqifu@nudt.edu.cn

¹College of Electronic Science and Technology, National University of Defense Technology, Changsha, 410073, China

Abstract

Rydberg atom-based superheterodyne with additional local oscillator (LO) signal is a novel approach to detect electric field with high measured sensitivity. However, the LO signal is often supplied to the atomic vapor cell by free-space illumination, which lacks mobility and integration for practical applications. Here, we present a LO port integrated split-ring resonator for realizing high sensitivity-enhanced electric field measurements. The LO signal is sent directly to the resonator through a parallel-plate waveguide, which is shown to achieve a sensitivity enhancement of 32 dB. The integrated resonator has an electrical size of 0.088λ and the feed port S11 reaches -38.2 dB.

Keywords: Rydberg atom-based metrology; Superheterodyne; Local oscillator port integrated

1 Introduction

With special properties not available in classical radio frequency (RF) microwave (MW) technology such as self-calibration [1, 2], high sensitivity [3, 4], and a wide range of operating frequencies [5–10], Rydberg atomic quantum metrology has been extensively pursued over the past decade, e.g., receivers for communication signals (amplitude modulated [8, 11–13], frequency modulated [14], phase modulated signals [15–17]), stereo players [18], spectrum analyzers [19, 20], Rydberg microwave-frequency-comb spectrometer [21], imaging [22, 23]. To further improve the measurement sensitivity, it has been proposed solutions including atomic superheterodyne receiver [24], enhanced metrology at the critical point of a many-body Rydberg atomic system [25], and resonator [26–31]. In the design of microwave aperture, some control is needed, such as metasurface [32, 33] control of electromagnetic wave, resonant cavity. These methods require local oscillator (LO) fields and mostly use free-space illumination. However, the mobility and integration in practical applications are constrained owing to the striking attenuation of the LO field during long-distance propagation, as well as multipath interference caused by scattering in real environments.

© The Author(s) 2024. **Open Access** This article is licensed under a Creative Commons Attribution 4.0 International License, which permits use, sharing, adaptation, distribution and reproduction in any medium or format, as long as you give appropriate credit to the original author(s) and the source, provide a link to the Creative Commons licence, and indicate if changes were made. The images or other third party material in this article are included in the article's Creative Commons licence, unless indicated otherwise in a credit line to the material. If material is not included in the article's Creative Commons licence and your intended use is not permitted by statutory regulation or exceeds the permitted use, you will need to obtain permission directly from the copyright holder. To view a copy of this licence, visit <http://creativecommons.org/licenses/by/4.0/>.

To effectively tackle these concerns and enhance the mobility, previous research [30] used the Rydberg superheterodyne system inside a parallel-plate waveguide (PPWG) configuration, utilizing the PPWG as a means to transmit the LO signal. However, it is noted that the electric field measurement improvement is merely 7.9 dB, suggesting a limited capability for enhancement. Paper [34] proposed an LO embedded field measurement enhancement resonator employing the PPWG antenna radiation and utilized cesium 60D state electromagnetically induced transparency (EIT) signal to detect 638 MHz MW field, where different $m_j = 1/2, 3/2, 5/2$ have different polarizability [35, 36]. If no polarizability value and analysis are used, this method may run the risk of generating mistakes in the computation of the E-field. The experimental setup enabled a significant E-field measurement enhancement of 34 dB and an electrical size of 0.342λ . However, it should also be mentioned that the S11 could only reach -0.11 dB, showing poor impedance matching ability. As a result, efficiently directed to the resonator configurations that can overcome attenuation with no multipath and improve S11 remain elusive.

In this paper, we propose an innovative design that integrates a PPWG with a split-ring resonator (SRR) resonant cavity. The proposed design comprises a resonator that has 32 dB electric (E) field improvement capacity and can effectively guide the LO signal to the resonator by PPWG. Here, we comprehensively analyze the PPWG transmission line LO port integrated methods of split-ring resonator. E field enhancement ability, S11-parameters and E field homogeneity of integrated resonator are investigated, and it is shown that S11-parameters result from numerous complicated factors, including the impedance matching [37] between the coax adapters and the PPWG, and feeding method for two ports. To overcome the gap in S11-parameters, we optimize the structure impedance matching and utilize a common mode signal to supply the LO port as the common mode impedance provides a better match for the port. Experimental measurements show that, the value of S11 is -38.2 dB, which is significantly lower than the previously reported S11 value of -0.11 dB in the literature [34]. Furthermore, employing PPWG transmission line integration without PPWG antenna radiation, the electrical size of the resonator is determined to be smaller 0.088λ . The findings may have implications for the mobility in practical scenarios.

2 Experimental setup

Figure 1 displays the main experimental setup. The energy level diagram in Fig. 1(a) illustrates the utilization of the EIT ladder approach [3, 38–40] to produce the Rydberg states of cesium (Cs) atoms within a vapor cell through two-photon transitions. This paper uses off-resonant Rydberg detection. Two laser sources are used: 852 nm has $1/e^2$ beam diameter of $800 \mu\text{m}$ with Rabi frequencies of about $2\pi \times 2.56$ MHz and approximately 509 nm has $1/e^2$ beam diameter of 1.4 mm with Rabi frequencies of about $2\pi \times 63.39$ MHz. The 852 nm laser frequency is locked to the $6S_{1/2} \rightarrow 6P_{3/2}$ transitions with Rabi frequency Ω_p . The 509 nm laser frequency is locked to the $6P_{3/2} \rightarrow 50S_{1/2}$ transitions with Rabi frequency Ω_c .

Figure 1(b) illustrates the configuration of the integrated resonator. The LO signal is effectively guided to the resonator via a planar parallel waveguide (PPWG). The integrated resonator is made of copper with silver plating on the outer surface to increase conductivity, and the loop has side lengths of 28×10 mm² and thickness of 2 mm. The PPWG is 47.6×10 mm². The vapor cell has an outer dimension of $10 \times 10 \times 10$ mm³ and 1 mm thick.

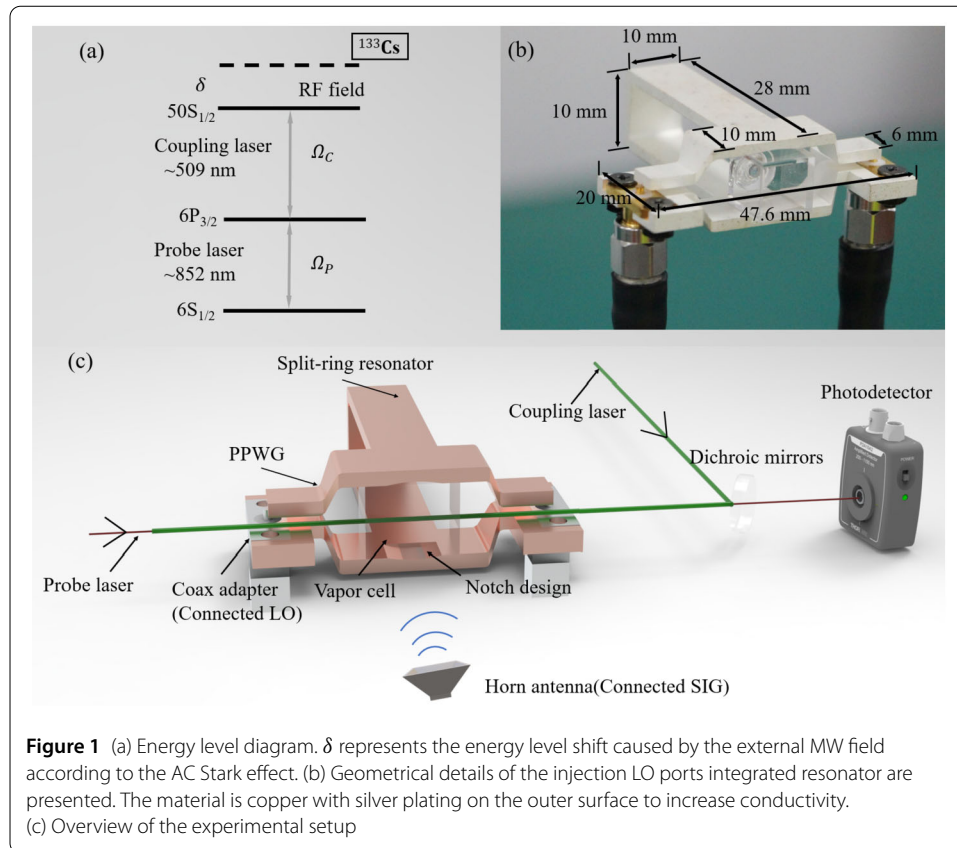
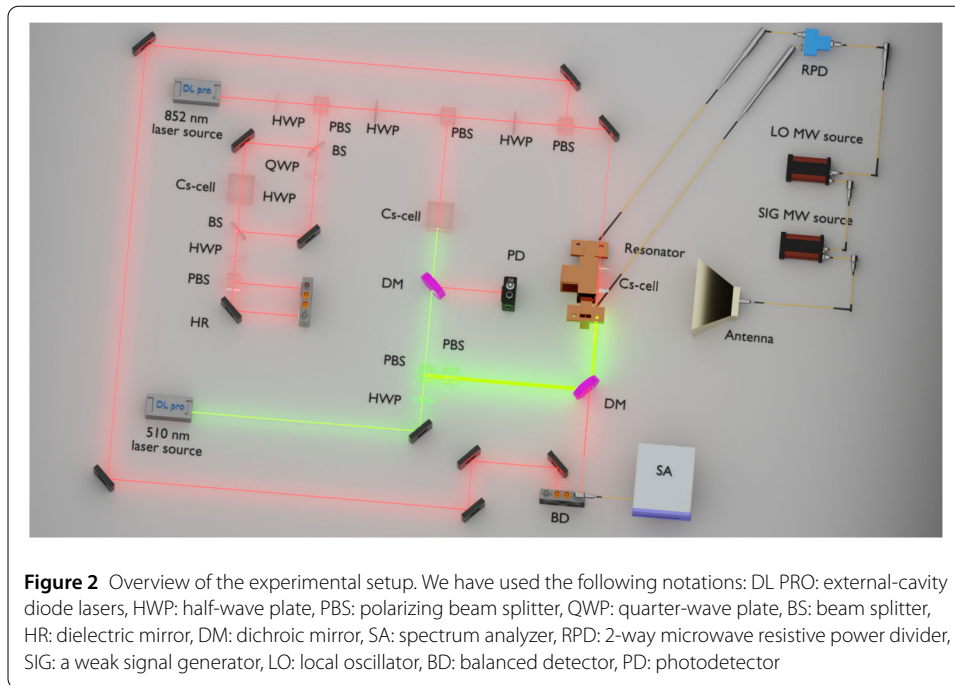


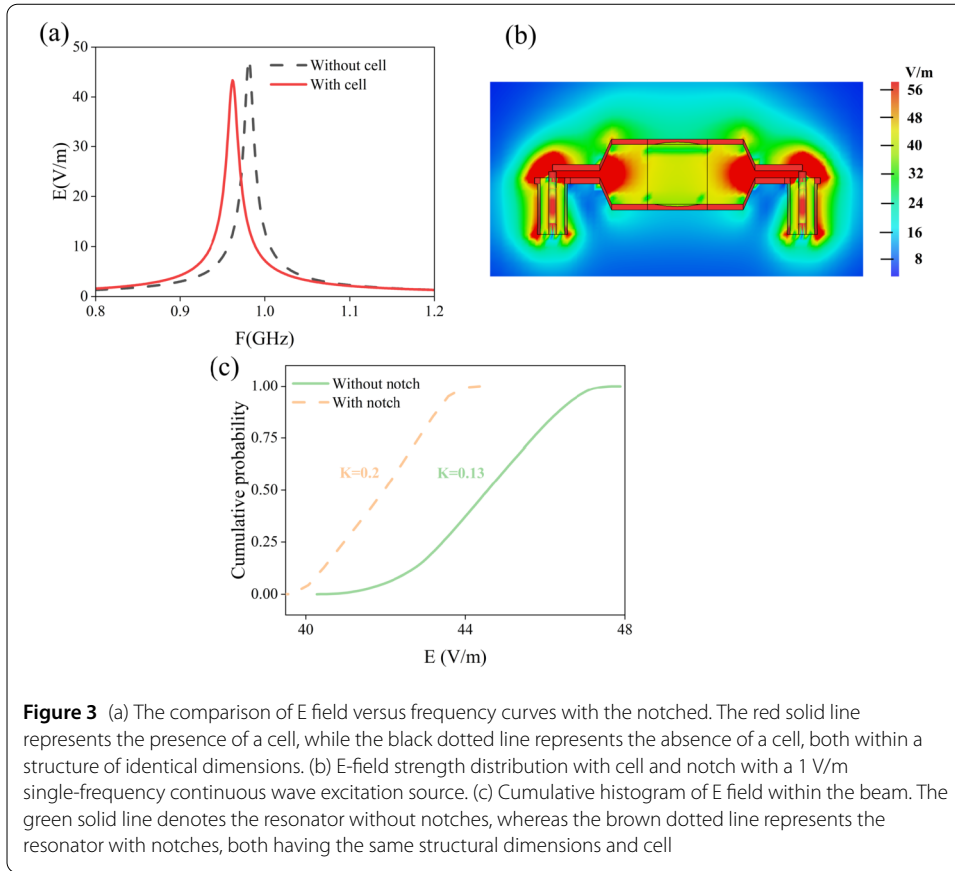
Figure 1(c) presents that a vapor cell is inserted into the LO ports integrated SRR. The probe laser, coupling laser are counter-propagating and coincide in the cesium vapor cell, and probe laser transmission is to be monitored on a photodetector at room temperature. The MW field is produced by using a weak signal generator (SIG) with a maximum output power of 25 dBm and is emitted via a horn antenna operating in the frequency range of 0.3-3 GHz. The LO signal is fed by two coax adapters using a common mode signal. The antenna is placed 20 cm in front of the vapor cell. SIG and LO MW fields irradiate into the atomic vapor cell with vertical polarization and propagate perpendicular to the propagation direction of the probe and coupling lasers. To stabilize the laser frequency, two Cs vapor cells are applied in the experiment. The probe laser is stabilized on the saturated absorption spectral signal of the Cs D2-line [41, 42]. Similarly, the coupling laser can be stabilized by the EIT signal generated by another vapor cell. The spectrum analyzer measures photodetector output voltage with a 1 Hz resolution bandwidth. Superheterodyne sensitivity is theoretically defined as the minimum detectable power when the Signal Noise Ratio(SNR) decreases to 1. The LO MW signal frequency is f , while the frequency of the weak SIG signal is detuned to $bf + 100$ kHz. The 100 kHz detuned frequency means that once the coupling laser is set, the probe laser intensity will oscillate at a beat-note frequency of 100 kHz. The results indicate that the Rydberg atom can achieve a function as a mixer [43], accurately down-convert the MW signal according to the frequency of the LO signal. The overall experimental scheme is illustrated in Fig. 2.

By comparison with and without cell scenario in Fig. 3(a), the resonant frequency experiences a downward trend from without cell to with cell regardless of considering ambient



factors. In general, the relative dielectric constant ϵ_r of cell wall is not equal to 1, which renders much larger electrical size. Changes, with and without cell in FDTD (Finite Difference Time-Domain Methods) simulations, the cell walls refractive index n ($n = \sqrt{\epsilon_r}$) parameter can greatly impact the resonant frequency, where ϵ_r is relative permittivity. Due to the small size of vapor-cell compared with the wavelength of the E field, the effects of the vapor cell on the measured MW E field are not significant [44].

The fundamental purpose of the LO ports integrated resonator is to ensure a significant rise in the E field at the selected cell position, minimize reflection, and achieve a uniform distribution of E-field. To acquire a major enhancement in the E field, we choose to integrate the PPWG at the open-ended of the SRR, which minimises the impact on the resonant cavity and transmission line. Additionally, to improve S11-parameters, it is also vital to optimise the impedance matching [37] between the coax adapters and the PPWG. Because the common mode impedance matches the port better, two coax adapters are fed the LO signal by utilizing a common mode signal with identical amplitude and phase to both feed ends simultaneously. Furthermore, achieving a uniform distribution of E field intensity for the LO signal throughout the PPWG is necessary. Homogeneous E field distribution represents a transmission line with Transverse Electric and Magnetic Field(TEM) wave uniform propagation for specified frequency range. To get homogeneous E field distribution, special structural design or a vapor cell perforated walls [45] can be used. Here we consider to add bilateral symmetrical notches on the top and bottom of the structure. Figure 3(b) illustrates the E field distribution with cell and notches in EastWave FDTD [46] simulation with a 1 V/m single-frequency continuous wave excitation source and linear polarization along the vertical direction. In the bottom panels, we present the cumulative histogram (Fig. 3(c)) generated by sampling a cylinder region of ten million samples in cell. The cylinder region with a length of 8 mm and a diameter of 0.5 mm, which is a reasonable size for the probe laser. Figure 3(c) shows the slopes(K) of with and without notches is 0.2



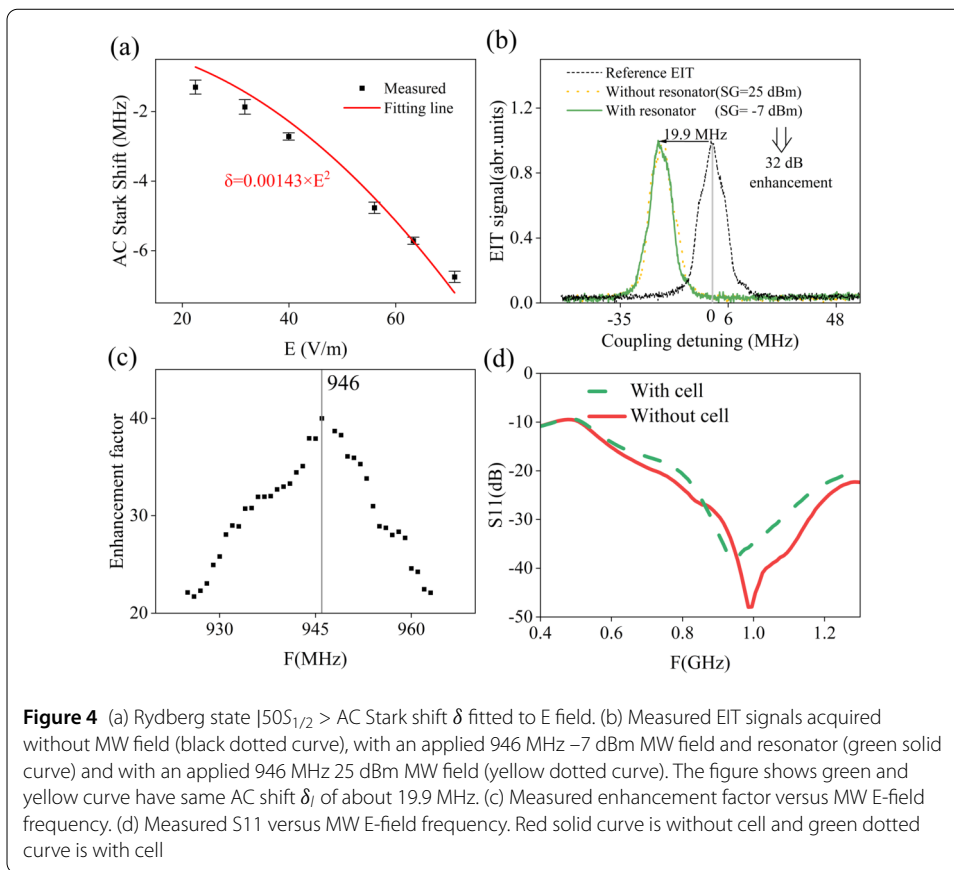
and 0.13, respectively. The FDTD simulation results clearly demonstrate the differences between the two scenarios, with notches distinctly improving the homogeneity of E-field.

3 Results and discussion

Off-resonant Rydberg atomic heterodyne approach [34–36, 47–50] has been employed. The presence of an applied MW E field causes an AC Stark shift in the Rydberg atomic energy level within the off-resonant region. The electric field strength E and the spectral shift δ follow quadratic correspondence [51]:

$$\delta = -\frac{E^2}{4}\alpha_0(\omega_{RF}) \tag{1}$$

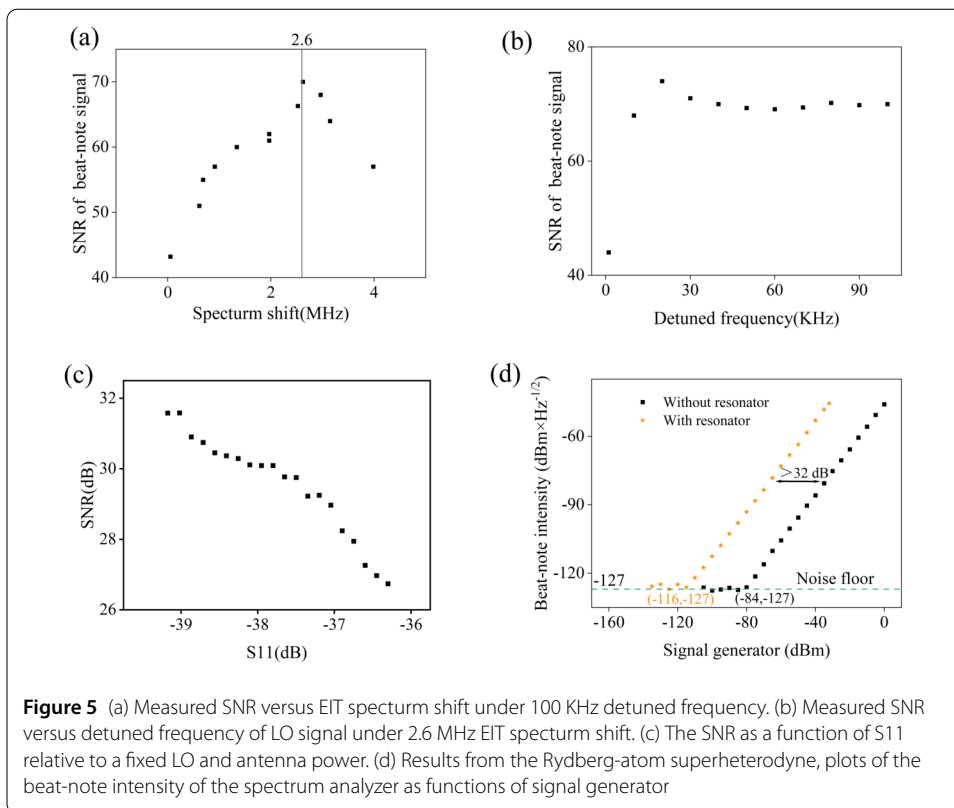
where $\alpha_0(\omega_{RF})$ is called as the AC dynamic scalar polarizability in the SI units of $\text{MHz}/(\text{V/m})^2$. In this study, we employ the cesium $50S_{1/2} m_j = 1/2$ state Electromagnetically Induced Transparency (EIT) signal to detect a MW field. The E field in the far off-resonant regime is primarily influenced by the polarizability $\alpha_0(\omega_{RF})$. Consequently, the usage of the 50D state EIT [34] has been precluded due to the significant variations in polarizability among different m_j values, namely $1/2, 3/2, \text{ and } 5/2$ [35, 36, 52]. The antenna radiation formula can be expressed as $|E| = \sqrt{\eta P \alpha G / 4\pi d^2}$ to calculate experimental E-fields, where $\eta = 377\Omega$ is the free space wave impedance, P is the output power of the signal generator, $\alpha = -0.8 \text{ dB}$ is the insertion loss between the analog signal generator and the antenna, $G = 7 \text{ dBi}$ is the gain of the antenna, and $d = 0.3\text{m}$ is the distance



from the antenna to the atomic-vapor cell. In the experiment, all the above parameters are constant, except for P . Consequently, the power P can be directly converted to the E-fields amplitudes. We calculate the $|50S_{1/2} \rangle$ Rydberg $\alpha_0 = 57\text{MHz} \cdot \text{cm}^2/\text{V}^2$ by fitting a quadratic relationship of the AC shift and the given RF E-field amplitudes as shown in Fig. 4(a). It is worth noting that the enhancement factor is calculated by comparing the SIG output power under the identical energy level shift with and without the resonator, with polarizability removed. As a result, the magnetic substates has virtually no effect on the enhancement factor.

Figure 4(b) shows Rydberg state EIT spectra (black dotted curve) in the state $|50S_{1/2} \rangle$ incident MW fields at 946 MHz, 25 dBm (yellow dotted curve) without resonator and -7 dBm (green solid curve) with resonator. Note that applied microwave field at 946 MHz induces a red-shift. By attenuating to 32 dBm after loading the resonator, the green and yellow curves showing the same AC shift Δ_l of 19.9 MHz, indicating the same observable E-field intensity. Thus, the resonator provides electric-field enhancement factor of $39.8(10^{(32/20)} = 39.8)$.

Figure 4(c) shows the evolutions of enhancement factor with the increment of microwave frequency where dots correspond to experimental results. We can clearly find that the resonator has a maximum measured E-field enhancement factor at 946 MHz and exhibits a fairly narrow frequency response. The resonant frequency shift from 962 MHz (FDTD simulation) to 946 MHz (experiment) can be attributed to the following: first, the cell inner surface has nonzero conductivity due to the adsorption of alkali-metal atoms [53] electric-field-screening effect. Second, the resonator metallic losses and minor differ-



ences in manufacturing dimensions may also lead to a reduction in the resonant frequency. Furthermore, scattering from the surroundings can alter the resonant frequency and E-field distribution.

Figure 4(d) shows S11 of the LO coax adapters versus MW frequency. By comparing S11 curves with and without cell, the resonant frequency falls in the presence of the cell. This transformation trend exhibits similarity to the one depicted in Fig. 3(a). By optimizing the impedance matching [37] between the coax adapters and the PPWG, S11 is improved to -38.2 dB. Thus, the optimized integrated resonator needs considerably less input power for the same field intensity within the specified frequency spectrum.

In order to improve the sensitivity of the E-field measurement when the SIG signal amplitude is fixed, we optimise various parameters [54, 55]. These include the LO signal amplitude (which is related to the EIT spectrum shifts shown in Fig. 5(a)) and the LO signal detuned frequency (Fig. 5(b)), as well as the power of the probe and coupling laser. As shown in Fig. 5(a), the SNR of beat-note signal curve has optimal points when EIT spectrum shift equals to 2.6 MHz. Figure 5(b) shows that SNR first rises and then plateaus as the detuned frequency increasing. We choose the 100 KHz detuned frequency.

To demonstrate the comparable sensitivities of the integrated LO to other SSRs with a smaller applied LO power, we present the SNR as a function of S11 relative to a fixed LO and antenna power in the 925 to 946 MHz frequency range, as shown in Fig. 5(c). The practical operational bandwidth for this system is 26 MHz. There is a significant increase in sensitivity in the 933 to 959 MHz frequency range. Figure 5(c) illustrates that the SNR falls from 31.6 dB to 26.7 dB the increment of S11. It is noteworthy that the low S11 in-

Table 1 Performance comparisons of Rydberg atom-based electric field measurement enhancement using resonators. Ref.: reference, f_0 : center frequency, ES: electrical size, EF: enhancement factor, S: sensitivity

Ref.	f_0	LO port	S11	ES	EF	S
[26, 27]	4.35 GHz	No	no mention	0.435λ	24 dB	no mention
[29]	1.309 GHz	No	no mention	0.096λ	40 dB	$5.5 \mu\text{V}/\text{cm}/\sqrt{\text{Hz}}$
[30]	19.629 GHz	Yes	no mention	3.273λ	7.9 dB	no mention
[34]	0.638 GHz	Yes	-0.1 dB	0.342λ	34 dB	$854 \text{ nV}/\text{cm}/\sqrt{\text{Hz}}$
This work	0.946 GHz	Yes	-38.2 dB	0.088λ	32 dB	$213 \text{ nV}/\text{cm}/\sqrt{\text{Hz}}$

indicates minimal reflection loss in this system, highlighting the integrated LO's ability to achieve equivalent sensitivities to other SSRs with reduced LO power.

As shown in Fig. 5(d), the beat-note intensity from the spectrum analyzer is a function of signal generator for the cases with resonator in yellow pentagrams and without in black dots. As indicated by the double-headed arrow, the two curves are shifted along the x-axis, suggesting an enhancement of 32 dB. This work identifies the intersections of the linear response curves and the noise floor of the spectrum analyzer as sensitivity. Ultimately, we find that the resonator provides a sensitivity of $213 \text{ nV}/\text{cm}/\sqrt{\text{Hz}}$; 40 times more sensitivity than without resonator ($8.13 \mu\text{V}/\text{cm}/\sqrt{\text{Hz}}$).

Table 1 summarizes the specific performance comparison with LO port integrated resonator in previous literatures [26, 27, 29, 30, 34]. Compared with the work in References [26, 27, 29], we provide a local oscillator port integrated resonator, which is more flexible for Rydberg atom-based superheterodyne. Compared with the work in References [26, 27, 29, 30, 34], the electrical size reaches a minimum of 0.088λ , which is critical for mobility in practical applications. Furthermore, the S11 decreases from -0.1 dB to -38.2 dB compared to the PPWG antenna radiation in Reference [34]. Furthermore, through the optimisation of experimental parameters, the sensitivity is successfully enhanced.

4 Conclusion

To summarize, LO port integrated resonator enables LO signal to be efficiently directed to the resonator through a PPWG. Results show that integrated resonator not only enhances mobility but also improves sensitivity by 32 dB. It is crucial for moving from laboratory to practical applications. Furthermore, the sensitivity is optimised through the optimisation of many parameters such as the LO signal amplitude, LO signal detuned frequency, and the power of the probe and coupling laser. Experiments have shown that sensitivity is $213 \text{ nV}/\text{cm}/\sqrt{\text{Hz}}$ in the off-resonant region. The electrical size is 0.088λ and S11 reaches -38.2 dB. This work paves the way for Rydberg atom-based superheterodyne incorporated with LO port integrated resonator to improve mobility in practical scenarios.

Funding

National Natural Science Foundation of China (Grant Nos. 12304436, 12104509 and 62105338), Natural Science Foundation of Hunan Province of China (Grants No.2022JJ40556).

Abbreviations

EIT, Electromagnetically Induced Transparency; RF, radio frequency; MW, microwave; PPWG, parallel-plate waveguide; SRR, split-ring resonator; SNR, signal to noise ratio; LO, local oscillator; SIG, weak signal; AT, Autler-Townes; Cs, cesium; TEM, Transverse Electric and Magnetic Field; Ref, reference; f_0 , center frequency; ES, electrical size; EF, enhancement factor; S, sensitivity; AC, alternating current.

Data availability

Data underlying the results presented in this paper are not publicly available at this time but may be obtained from the authors upon reasonable request.

Declarations

Competing interests

The authors declare no competing interests.

Author contributions

Bo Wu and Yun-qi Fu constructed the theoretical scheme, Bo Wu wrote the main manuscript text, Zhen-ke Ding, Dun-wei Liao, Kai Yang, Yi Liu and Qiang An gave some important suggestions about the calculation methods and Yun-qi Fu made the final revisions. All authors reviewed and approved the final manuscript.

Received: 30 October 2023 Accepted: 7 March 2024 Published online: 22 March 2024

References

1. Sedlacek JA, Schwettmann A, Kübler H, Löw R, Pfau T, Shaffer JP. Microwave electrometry with Rydberg atoms in a vapour cell using bright atomic resonances. *Nat Phys.* 2012;8(11):819–24.
2. Yang K, Mao R, An Q, Sun Z, Fu Y. Laser frequency locking method for Rydberg atomic sensing. *Chin Opt Lett.* 2023;21(2):021407.
3. Holloway CL, Simons MT, Gordon JA, Dienstfrey A, Anderson DA, Raithel G. Electric field metrology for si traceability: systematic measurement uncertainties in electromagnetically induced transparency in atomic vapor. *J Appl Phys.* 2017;121(23):233106.
4. Yao J, An Q, Zhou Y, Yang K, Wu F, Fu Y. Sensitivity enhancement of far-detuned rf field sensing based on Rydberg atoms dressed by a near-resonant rf field. *Opt Lett.* 2022;47(20):5256–9.
5. Holloway CL, Gordon JA, Jefferts S, Schwarzkopf A, Anderson DA, Miller SA, Thaicharoen N, Raithel G. Broadband Rydberg atom-based electric-field probe for si-traceable, self-calibrated measurements. *IEEE Trans Antennas Propag.* 2014;62(12):6169–82.
6. Calero V, Fernández-Mateo R, Morgan H, García-Sánchez P, Ramos A. Stationary electro-osmotic flow driven by ac fields around insulators. *Phys Rev Appl.* 2021;15(1):014047.
7. Cui Y, Jia F-D, Hao J-H, Wang Y-H, Zhou F, Liu X-B, Yu Y-H, Mei J, Bai J-H, Bao Y-Y et al. Extending bandwidth sensitivity of Rydberg-atom-based microwave electrometry using an auxiliary microwave field. *Phys Rev A.* 2023;107(4):043102.
8. Simons MT, Artusio-Glimpse AB, Holloway CL, Imhof E, Jefferts SR, Wylie R, Sawyer BC, Walker TG. Continuous radio-frequency electric-field detection through adjacent Rydberg resonance tuning. *Phys Rev A.* 2021;104(3):032824.
9. Liu X-H, Liao K-Y, Zhang Z-X, Tu H-T, Bian W, Li Z-Q, Zheng S-Y, Li H-H, Huang W, Yan H et al. Continuous-frequency microwave heterodyne detection in an atomic vapor cell. *Phys Rev Appl.* 2022;18(5):054003.
10. Mao R, Lin Y, Fu Y, Ma Y, Yang K. Digital beamforming and receiving array research based on Rydberg field probes. *IEEE Trans Antennas Propag.* 2024;72:2025–9.
11. Meyer DH, Cox KC, Fatemi FK, Kunz PD. Digital communication with Rydberg atoms and amplitude-modulated microwave fields. *Appl Phys Lett.* 2018;112(21):211108.
12. Liu X, Jia F, Zhang H, Mei J, Yu Y, Liang W, Zhang J, Xie F, Zhong Z. Using amplitude modulation of the microwave field to improve the sensitivity of rydberg-atom based microwave electrometry. *AIP Adv.* 2021;11(8).
13. Yang K, Sun Z, Mao R, Lin Y, Liu Y, An Q, Fu Y. Wideband Rydberg atom-based receiver for amplitude modulation radio frequency communication. *Chin Opt Lett.* 2022;20(8):081203.
14. Anderson DA, Sapiro RE, Raithel G. An atomic receiver for am and fm radio communication. *IEEE Trans Antennas Propag.* 2020;69(5):2455–62.
15. Song Z, Liu H, Liu X, Zhang W, Zou H, Zhang J, Qu J. Rydberg-atom-based digital communication using a continuously tunable radio-frequency carrier. *Opt Express.* 2019;27(6):8848–57.
16. Zhang Q, Wu X, Qin S. Pressure-induced phase transition in transition metal trifluorides. *Chin Phys B.* 2017;26(9):090703.
17. Jia F, Zhang H, Liu X, Mei J, Yu Y, Lin Z, Dong H, Liu Y, Zhang J, Xie F. Transfer phase of microwave to beat amplitude in a Rydberg atom-based mixer by Zeeman modulation. *J Phys B, At Mol Opt Phys.* 2021;54(16):165501.
18. Holloway CL, Simons MT, Gordon JA, Novotny D. Detecting and receiving phase-modulated signals with a Rydberg atom-based receiver. *IEEE Antennas Wirel Propag Lett.* 2019;18(9):1853–7.
19. Holloway C, Simons M, Haddab AH, Gordon JA, Anderson DA, Raithel G, Voran S. A multiple-band Rydberg atom-based receiver: am/fm stereo reception. *IEEE Antennas Propag Mag.* 2020;63(3):63–76.
20. Meyer DH, Castillo ZA, Cox KC, Kunz PD. Assessment of Rydberg atoms for wideband electric field sensing. *J Phys B, At Mol Opt Phys.* 2020;53(3):034001.
21. Zhang L, Liu Z, Liu B, Zhang Z, Guo G, Ding D, Shi B. Rydberg microwave-frequency-comb spectrometer. *Phys Rev Appl.* 2022;18:014033.
22. Fan H, Kumar S, Daschner R, Kübler H, Shaffer J. Subwavelength microwave electric-field imaging using Rydberg atoms inside atomic vapor cells. *Opt Lett.* 2014;39(10):3030–3.
23. Mao R, Lin Y, Yang K, An Q, Fu Y. SA high-efficiency fiber-coupled Rydberg-atom integrated probe and its imaging applications. *IEEE Antennas Wirel Propag Lett.* 2023;22(2):352–6.
24. Jing M, Hu Y, Ma J, Zhang H, Zhang L, Xiao L, Jia S. Atomic superheterodyne receiver based on microwave-dressed Rydberg spectroscopy. *Nat Phys.* 2020;16(9):911–5.
25. Ding D, Liu Z, Shi B, Guo G, Mølmer K, Adams CS. Enhanced metrology at the critical point of a many-body Rydberg atomic system. *Nat Phys.* 2022;18(12):1447–52.
26. Anderson DA, Paradis EG, Raithel G. A vapor-cell atomic sensor for radio-frequency field detection using a polarization-selective field enhancement resonator. *Appl Phys Lett.* 2018;113(7):073501.
27. Anderson DA, Raithel GA, Paradis EG, Sapiro RE. Atom-based electromagnetic field sensing element and measurement system. 2019. CA3085935.
28. Wu B, Lin Y, Liao D, Liu Y, An Q, Fu Y. Design of locally enhanced electric field in dielectric loaded rectangular resonator for quantum microwave measurements. *Electron Lett.* 2022;58(24):914–6.
29. Holloway CL, Prajapati N, Artusio-Glimpse AB, Berweger S, Simons MT, Kasahara Y, Andrea ZRW. Rydberg atom-based field sensing enhancement using a split-ring resonator. *Appl Phys Lett.* 2022;120(20):204001.

30. Simons MT, Haddab AH, Gordon JA, Novotny D, Holloway CL. Embedding a Rydberg atom-based sensor into an antenna for phase and amplitude detection of radio-frequency fields and modulated signals. *IEEE Access*. 2019;7:164975–85.
31. Wu B, Lin Y, Wu F, Chen X, An Q, Liu Y, Fu Y. Quantum microwave electric field measurement technology based on enhancement electric field resonator. *Acta Phys Sin*. 2023;72:034204.
32. Tian T, Huang X, Xu Y, Liu P, Liu C, Hu N, Zhang J, Wu Z. A wideband energy selective surface with quasi-elliptic bandpass response and high-power microwave shielding. *IEEE Trans Electromagn Compat*. 2024;66:224.
33. Wen K, Huang X, Tian T, Huang W, Liu P. Design and demonstration of high-power density infrared nonlinear filtering window with EM shielding. *Opt Express*. 2024;32:5956–68.
34. Yang K, Mao R, He L, Yao J, Li J, Sun Z, Fu Y. Local oscillator port embedded field enhancement resonator for Rydberg atomic heterodyne technique. *EPJ Quantum Technol*. 2023;10:23.
35. Hu J, Li H, Song R, Bai J, Jiao Y, Zhao J, Jia S. Continuously tunable radio frequency electrometry with rydberg atoms. *Appl Phys Lett*. 2022;121(1).
36. Jiao Y, Hao L, Han X, Bai S, Raithe G, Zhao J, Jia S. Atom-based radio-frequency field calibration and polarization measurement using cesium n D j Floquet states. *Phys Rev Appl*. 2017;8(1):014028.
37. Zdeněk K, Denys N, Pavel K, Jiří S, Miroslav H. Optimization of electrical properties of parallel plate antenna for emc testing. *J Comput Appl Math*. 2014;270:283–93.
38. Zhang L, Jia Y, Jing M, Guo L, Zhang H, Xiao L, Jia S. Detuning radio-frequency electrometry using Rydberg atoms in a room-temperature vapor cell. *Laser Phys*. 2019;29:035701.
39. Kumar S, Fan H, Kübler H, Sheng J, Shaffer JP. Atom-based sensing of weak radio frequency electric fields using homodyne readout. *Sci Rep*. 2017;7:42981.
40. Zou H, Song Z, Mu H, Feng Z, Qu J, Wang Q. Atomic receiver by utilizing multiple radio-frequency coupling at Rydberg states of rubidium. *Appl Sci*. 2020;10:1346.
41. Zhang P, Jing M, Wang Z, Peng Y, Yuan S, Zhang H, Xiao L, Jia S, Zhang L. Quantum scaling atomic superheterodyne receiver. *EPJ Quantum Technol*. 2023;10(1):39.
42. Wu B, Yao J, Wu F, An Q, Fu Y. Dependence of Rydberg-atom-based sensor performance on different Rydberg atom populations in one atomic-vapor cell. *Chin Phys B*. 2024;33:024205.
43. Simons MT, Haddab AH, Gordon JA, Holloway CL. A Rydberg atom-based mixer: measuring the phase of a radio frequency wave. *Appl Phys Lett*. 2019;114:114101.
44. Fan H, Kumar S, Sheng J, Shaffer JP, Holloway CL, Gordon JA. Effect of vapor-cell geometry on Rydberg-atom-based measurements of radio-frequency electric fields. *Phys Rev Appl*. 2015;4:044015.
45. Ripka F, Amarloo H, Keaveney J, Gillet G, Kübler H, Shaffer JP. Application-driven problems in Rydberg atom electrometry. In: *Optical and quantum sensing and precision metrology*. 2021.
46. Lu J, Ni T, Yu Z, Wang J, Qi D, Bin C. Research on electromagnetic environment of shipborne shortwave antenna based on eastwave. In: *2022 IEEE 5th International Conference on Electronic Information and Communication Technology (ICEICT)*. 2022. p. 769–71.
47. Liu B, Zhang L, Liu Z, Zhang Z, Zhu Z, Gao W, Guo G, Ding D, Shi B. Highly sensitive measurement of a megahertz rf electric field with a Rydberg-atom sensor. *Phys Rev Appl*. 2022;18:014045.
48. Miller SA, Anderson DA, Raithe G. Radio-frequency-modulated Rydberg states in a vapor cell. *New J Phys*. 2016;18:053017.
49. Anderson DA, Miller SA, Raithe G, Gordon JA, Butler ML, Holloway CL. Optical measurements of strong microwave fields with Rydberg atoms in a vapor cell. *Phys Rev Appl*. 2016;5:034003.
50. You SH, Cai MH, Zhang SS, Xu ZS, Liu HP. Microwave-field sensing via electromagnetically induced absorption of rb irradiated by three-color infrared lasers. *Opt Express*. 2022;30(10):16619–29.
51. Cardman R, Gonçalves LF, Sapiro RE, Raithe G, Anderson DA. Atomic 2d electric field imaging of a Yagi–Uda antenna near-field using a portable Rydberg-atom probe and measurement instrument. *Adv Opt Technol*. 2020;9:305–12.
52. Šibalić N, Pritchard JD, Adams CS, Weatherill KJ. Arc an open-source library for calculating properties of alkali Rydberg atoms. *Comput Phys Commun*. 2017;220:319–31.
53. Jau Y, Carter T. Vapor cell based atomic electrometry for detection frequencies below 1 khz. *Phys Rev Appl*. 2020;13(5):054034.
54. Cai M, You S, Zhang S, Xu Z, Liu H. Sensitivity extension of atom-based amplitude-modulation microwave electrometry via high Rydberg states. *Appl Phys Lett*. 2023;122:161103.
55. Cai M, Xu Z, You S, Liu H. Sensitivity improvement and determination of Rydberg atom-based microwave sensor. *Photonics*. 2022;9:250.

Publisher's Note

Springer Nature remains neutral with regard to jurisdictional claims in published maps and institutional affiliations.